



PERGAMON

---

**CORROSION  
SCIENCE**

---

Corrosion Science 41 (1999) 421–438

## Localized corrosion of 2024 T351 aluminium alloy in chloride media

Valérie Guillaumin\*, Georges Mankowski

*Laboratoire de Cristallochimie, Réactivité et Protection des Matériaux, UPRESA CNRS 5071, ENSCT,  
118 route de Narbonne, 31077 Toulouse Cedex 04, France*

Received 22 April 1998; accepted 22 July 1998

---

### Abstract

The corrosion behaviour of 2024 T351 alloy was studied in chloride solutions. The polarization curve of this alloy showed two breakdown potentials. The first was related to the dissolution of the coarse intermetallic Al<sub>2</sub>CuMg particles. A severe Mg dealloying of the particles resulted in Cu-rich remnants. The matrix surrounding the particles was systematically found to be dissolved. Indeed, the particles are surrounded by a dispersoid-free zone which is anodic in comparison to both the rest of the matrix and the S phase particles. The second breakdown potential corresponded to the matrix breakdown potential. Pits but also intergranular corrosion developed. Grain boundaries were preferentially attacked because they are anodic in comparison to the grain body and the previous dissolution of the intergranular precipitates made them fragile. © 1999 Elsevier Science Ltd. All rights reserved.

*Keywords:* Al 2024; Pitting corrosion; Intergranular corrosion; Intermetallics

---

### 1. Introduction

Because of its high mechanical performance and its low density, 2024 T3 alloy is used in the aircraft industry for numerous applications such as fuselage and door skin, dorsal fin and trailing edge panels. Nevertheless, this alloy can be affected by different forms of corrosion like pitting corrosion, intergranular corrosion, stress corrosion cracking or exfoliation corrosion.

It is generally accepted that intergranular corrosion is caused by the development along the grain boundary of an adjacent denuded zone during the precipitation of intermetallic second-phase precipitates in the grain boundary [1]. If the boundary

---

\* Corresponding author.

Table 1  
Composition of 2024 T351 alloy (wt%)

	Al	Si	Fe	Cu	Mn	Mg	Cr	Zn	Ti
2024 T351	base	0.06	0.17	4.54	0.63	1.51	0.01	0.08	0.03

precipitates are anodic toward the matrix and the precipitate free zone, they preferentially dissolve; in the opposite case, the adjacent denuded zone is attacked. Galvele and De Micheli [2] have studied the influence of chloride ions on the intergranular corrosion of Al-Cu alloys and showed that intergranular attack is not due to a difference in corrosion potentials between grain boundary and grain bodies, but to a difference in the breakdown potentials of these phases.

Other investigators [3–5] have shown that the anodic nature of the grain boundary region can be attributed to a high concentration of solute atoms in these regions as compared to grain interiors.

In this study, the corrosion behaviour of 2024 T351 alloy was investigated in 1 M NaCl solution. The purpose of this work was to understand the susceptibility of the alloy towards intergranular corrosion and other localized corrosion from potentiokinetic polarization curves. Specific attention was given to coarse Cu-Mg-rich particles whose corrosion behaviour explains changes occurring in the polarization curves.

## 2. Experimental method

### 2.1. Material

Corrosion investigations were performed on 2024 T351 alloy supplied in the form of a 25 mm thick plate. Its composition is given in Table 1. Specimens were prepared by cutting coupons of  $10 \times 10 \text{ mm}^2$  from the alloy plates. The edges of the specimens were covered with varnish, leaving a rolling plane area of  $100 \text{ mm}^2$  uncovered. Before testing, the samples were mechanically polished with 4000 grit SiC paper, and then with  $1 \mu\text{m}$  diamond paste. They were finally rinsed with distilled water.

### 2.2. Potentiodynamic test

All measurements were made at room temperature in naturally aerated 1 M NaCl ( $\text{pH}=6$ ). The tests consisted of potentiokinetic polarization of the samples from the cathodic potential of  $-900 \text{ mV/SCE}$  to the highest potential of  $-400 \text{ mV/SCE}$ . The potential sweep rate was  $500 \text{ mV/h}$ . All potentials quoted are relative to the saturated calomel electrode, the counter electrode was platinum.

### 2.3. Potentiostatic tests

For several tests, the scanning potential was stopped at a given value, and the specimens were maintained at this final potential during various times. The current versus time was recorded.

### 2.4. Phase shifting interferometric microscopy [6]

This method, based on classical interferometry, was used to study the behaviour of intermetallic particles through 2D and 3D profiles. As accurate repositioning of the samples was possible, the profiles plotted before and after the test were compared. This technique was chosen since the lateral resolution was well suited to the dimensions of the intermetallic particles; on the other hand, the resolution in depth was very high: 1 nm. Consequently, even slight modifications occurring in the shape of the precipitates or in the matrix around them can be measured.

### 2.5. Microscopic observations

After polarization, specimens were firstly examined by optical microscopy. Then, observations by scanning electron microscopy (SEM) were performed with a JEOL JXA 6400 in order to study the behaviour of the intermetallic particles. SEM also allowed the observation and the localization of pits or intergranular attack if the potential reached during the corresponding test was sufficiently high to allow pitting corrosion and intergranular corrosion. Observations by transmission electron microscopy (TEM) were also performed using a JEOL JM 2010, in order to examine intergranular precipitation and very small particles.

### 2.6. Analysis

Finally, energy dispersed spectrometry (EDS) analysis was performed during SEM observations to study the evolution of the intermetallic particle composition at different potentials. Likewise, EDS analysis during TEM observations was used to determine the composition of intergranular and other small precipitates.

## 3. Experimental results and discussion

### 3.1. Microstructure

Susceptibility to intergranular corrosion and to other localized corrosion forms depends on the alloy microstructure.

The rolled high-strength 2024 T351 alloy presents a grain size range between 50 µm and 700 µm; obviously, the grains are elongated in the rolling direction. Both optical and SEM observations performed on alloy 2024 T351 show the presence of a uniform

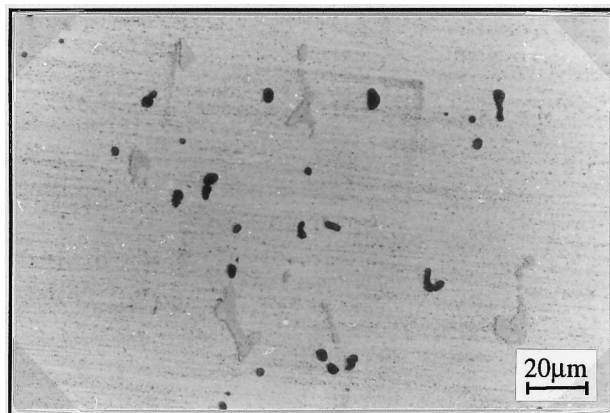


Fig. 1. Coarse intermetallic particles in 2024 T351 alloy. Black: Al-Cu-Mg-containing particles; Grey: Al-Cu-Mn-Fe-containing particles.

distribution of coarse intermetallic particles throughout (Figure 1). They are very large, their size reaching 30  $\mu\text{m}$ . The EDS analysis of these second phase particles allows two types of precipitates to be distinguished: more or less spherical Al-Cu-Mg-containing particles and very large and irregularly shaped Al-Cu-Mn-Fe-containing particles. Such intermetallic particles have also been observed by other authors [7–11]. The first type was assigned [7, 8] to the  $\text{Al}_2\text{CuMg}$  chemical combination (S phase), whereas the assignment of the second one was difficult. Indeed, EDS analysis revealed to different chemical phases [7]:  $\text{Al}_6(\text{Cu},\text{Fe},\text{Mn})$ ,  $\text{Al}_7\text{Fe}_2\text{Cu}$ , or  $(\text{Al},\text{Cu})_6\text{Mn}$ .

Observations by TEM were performed to reveal smaller particles. EDS analysis was also used to determine their chemical composition. In the matrix, we found:

- needle shaped hardening precipitates with a long side of around 100 nm (Figure 2). They can be assigned to the hardening phase  $\text{Al}_2\text{CuMg}$ . In Fig. 2, no precipitate-free zone can be observed along the grain boundary.
- rod shaped dispersoids with an average length of 200 nm. They can be assigned to the  $\text{Al}_{20}\text{Mn}_3\text{Cu}_2$  phase and their distribution is very homogeneous throughout the matrix. However, all the coarse intermetallic particles are surrounded by a  $\text{Al}_{20}\text{Mn}_3\text{Cu}_2$  dispersoid-free zone: Fig. 3 shows an  $\text{Al}_2\text{CuMg}$  particle surrounded by a dispersoid-free zone. These dispersoids are again encountered around 500 nm from the coarse intermetallic particle. In Fig. 4, six Al-Cu-Mn-Fe-containing particles are close to each other. All the matrix surrounding these coarse intermetallic particles is also free of dispersoids. At the top of the TEM micrograph, there are no more coarse particles, and hence, the matrix presents a homogeneous distribution of dispersoids.

In the grain boundary, we found:

- hardening  $\text{Al}_2\text{CuMg}$  precipitates which were encountered in the matrix (Figure 5).
- bigger needle shaped particles with an average length of 100 nm containing Al,

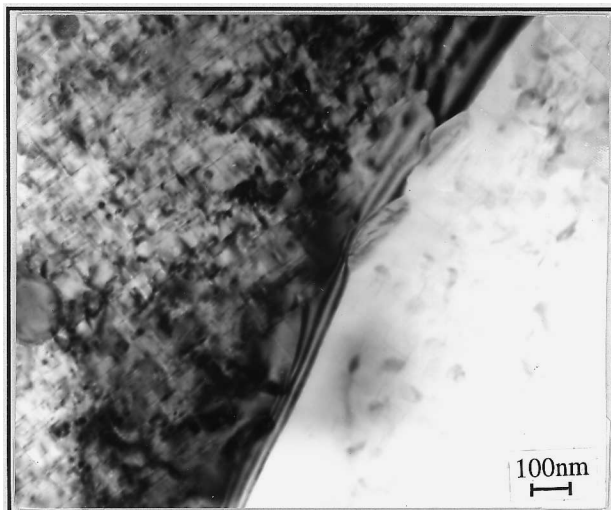


Fig. 2. Hardening  $\text{Al}_2\text{CuMg}$  precipitates in the matrix close to a grain boundary.

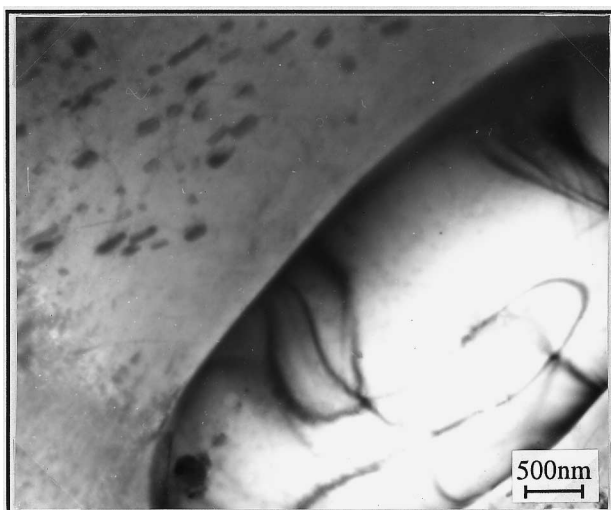


Fig. 3. Coarse intermetallic  $\text{Al}_2\text{CuMg}$  particle surrounded by a  $\text{Al}_{20}\text{Mn}_3\text{Cu}_2$  dispersoid-free zone.

Cu, Mg (Figure 6) which can be assigned to the  $\text{Al}_2\text{CuMg}$  chemical combination (S phase).

Both dispersoids and intergranular precipitates have also been observed and analysed by various authors [8, 12–14].

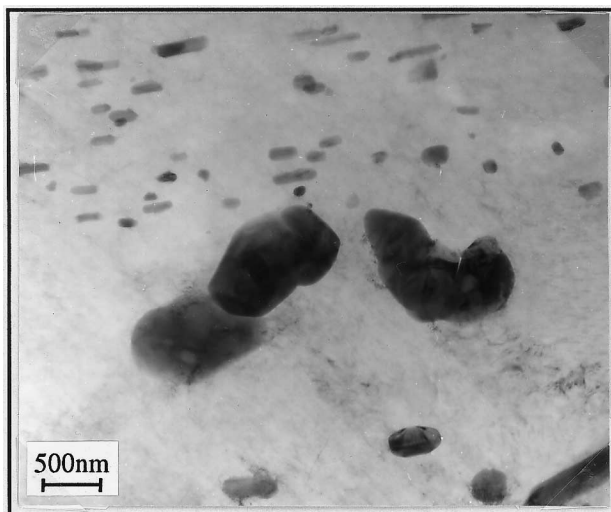


Fig. 4. Al-Cu-Mn-Fe-containing particles surrounded by a  $\text{Al}_{20}\text{Mn}_3\text{Cu}_2$  dispersoid-free zone.

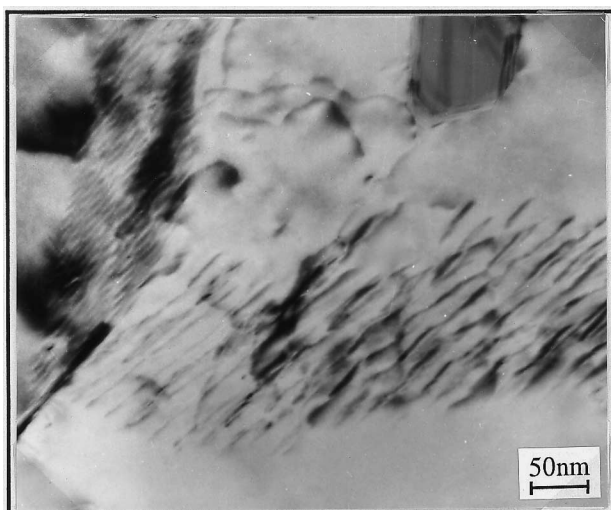


Fig. 5. Hardening  $\text{Al}_2\text{CuMg}$  precipitates in the grain boundary.

### 3.2. Polarization curve in sodium chloride solution and breakdown potential

Figure 7 shows a typical example of a potentiokinetic polarization curve obtained in 1 M NaCl solution for alloy 2024 T351. The curve shows two breakdown potentials: the more active one  $E_{b1}$ , close to  $-720$  mV and the more noble one  $E_{b2}$ , close to  $-620$  mV. Each of these breakdown potentials presents a rapid rise in anodic current density.

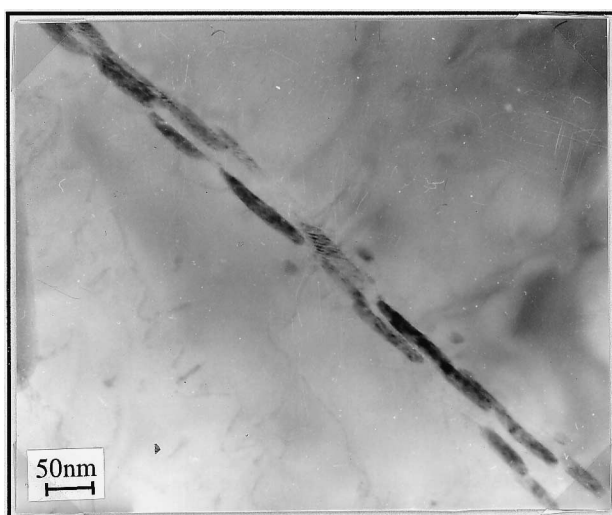


Fig. 6. Al<sub>2</sub>CuMg precipitates (S phase) in the grain boundary.

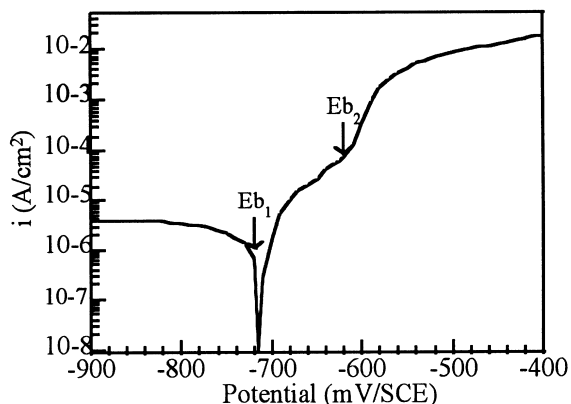


Fig. 7. Potentiokinetic polarization curve of 2024 T351 alloy in 1 M NaCl solution.

As previously explained [5], the breakdown potential corresponds to the dissolution potential of a metallurgical phase. The polarization curve of a given alloy containing more than one phase may indicate the breakdown potential of each phase, if these breakdown potentials are sufficiently different. Therefore, the polarization curve of the given alloy consists of a sequence of rapid rises in current density, each separated by a region of current stabilisation the length of which depends on the difference between the breakdown potential values. In the polarization curve of 2024 T351 alloy Figure 7, current stabilisation is not very clear. Indeed, only 100 mV separate the two breakdown potentials,  $E_{b1}$  and  $E_{b2}$ .

Galvele and De Micheli [2] have shown that two breakdown potentials can be

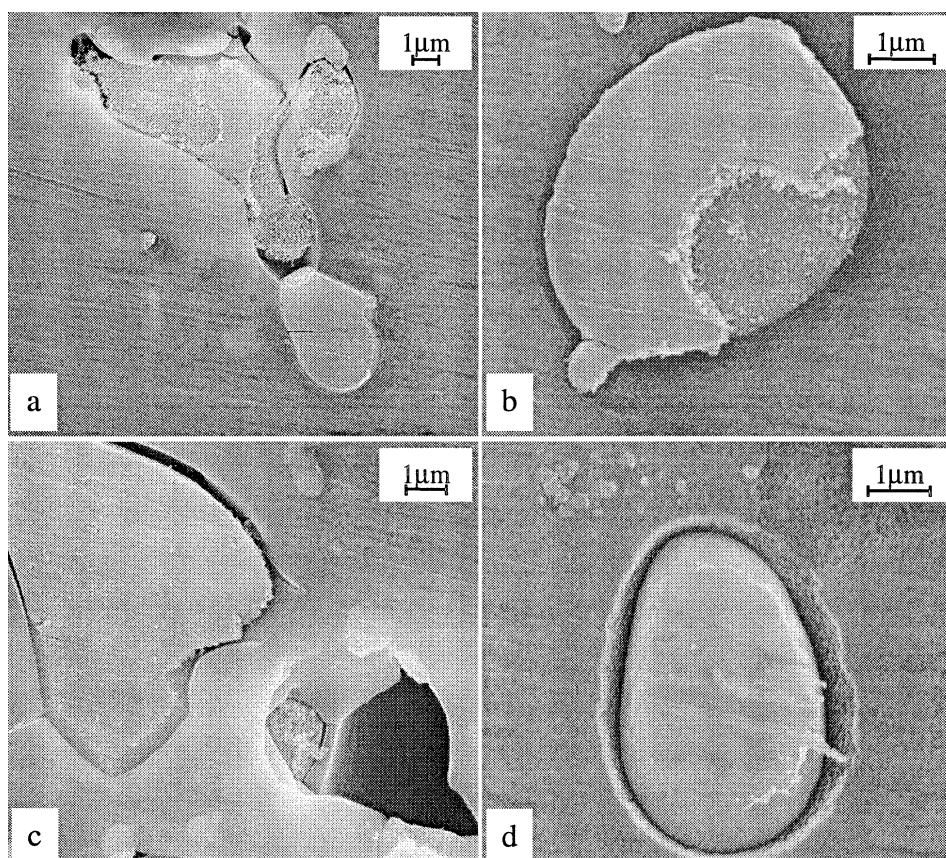


Fig. 8. S phase particles after potentiokinetic polarization to  $-690\text{ mV/SCE}$ , the potential was maintained at  $-690\text{ mV/SCE}$  for 5 mn.

found in the anodic polarization curve of an aged Al-4%Cu alloy in deaerated 1 M NaCl solution. The lower one corresponds to the dissolution of the Cu-depleted zone along the grain boundary and the higher one corresponds to the dissolution of the grain bodies.

Obviously, below the breakdown potential, the rate of dissolution of the corresponding phase is low. When the breakdown potential is reached, the dissolution rate increases and the phase can be seriously attacked.

### 3.3. First breakdown potential: Cu-Mg-rich intermetallic particle behaviour

In Fig. 8, four micrographs show the remnant S phase particles after potentiokinetic polarization to  $-690\text{ mV}$  (i.e. 30 mV higher than the first breakdown potential). Some particles were severely attacked, and a resulting sponge-like structure covered by a more homogeneous layer can be observed (Figure 8a and Fig. 8b); other particles fell

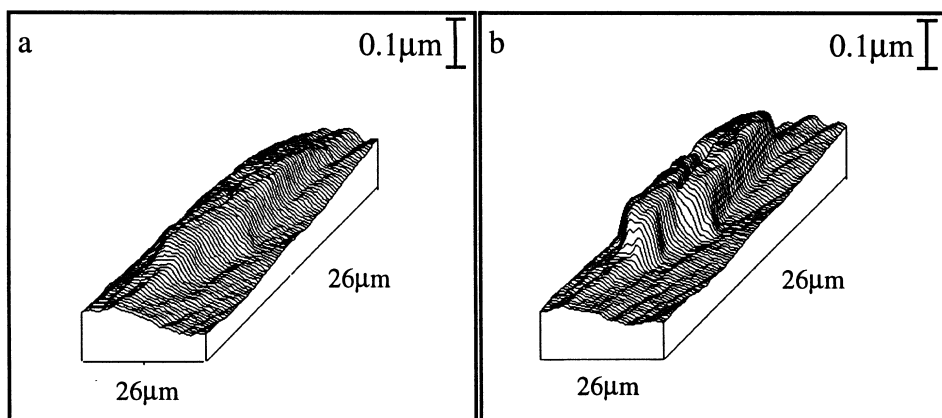


Fig. 9. 3D profiles of an Al-Cu-Mn-Fe containing particle: a-after polishing; b-after 5 mn of polarization at  $-750\text{ mV/SCE}$ .

out or were entirely dissolved (hole in Fig. 8c). Some S phase particles seem to be partially dissolved (Figure 8a), others remain largely intact (Figure 8a and Fig. 8d). As clearly shown in Fig. 8d, in the vicinity of the particles, the surrounding matrix was systematically found to be locally dissolved (Figure 8d). On the contrary, the Al-Cu-Mn-Fe-containing particles, the matrix and the grain boundary remain unattacked.

To study the behaviour of the coarse intermetallic particles in detail, phase shifting interferometric microscopy was performed on alloy 2024 T351. On and after  $E_{b1}$ , S phase particles dissolution was so strong that it was not possible to use PSIM. So, to characterise the reactivity of coarse intermetallic particles, the specimen was polarized for 5 mn at  $-750\text{ mV}$ , i.e. 30 mV lower than the first breakdown potential  $E_{b1}$ . Figure 9b and Fig. 10b show the 3D profiles plotted for a Al-Cu-Mn-Fe containing particle and for a  $\text{Al}_2\text{CuMg}$  particle respectively after 5 mn at  $-750\text{ mV}$ , in 1 M NaCl solution. The 3D profiles plotted before polarization are shown in Fig. 9a and Fig. 10a. In Fig. 9a, the Al-Cu-Mn-Fe containing particle appears in relief whereas in Fig. 10a, the  $\text{Al}_2\text{CuMg}$  particle appears as a hollow. This is due to the differences of hardness between the matrix and the coarse intermetallic particles which leads to such particle relief after polishing. Figure 11 shows the 2D profiles of the same S phase particle shown in Fig. 10.

— comparison of Fig. 9a and Fig. 9b shows no significant modification of the Al-Cu-Mn-Fe-containing particle. Nevertheless, the particle has a more strongly marked relief. This indicates that at potentials lower than  $E_{b1}$ , the matrix dissolves slightly over the whole specimen surface whereas the particle seems to remain undamaged.

— comparison of Fig. 10a and Fig. 10b corroborates the hypothesis of matrix dissolution over the specimen surface. Indeed, the S phase particle seems to inflate. The slight dissolution of the whole matrix can be due to the fact that when the

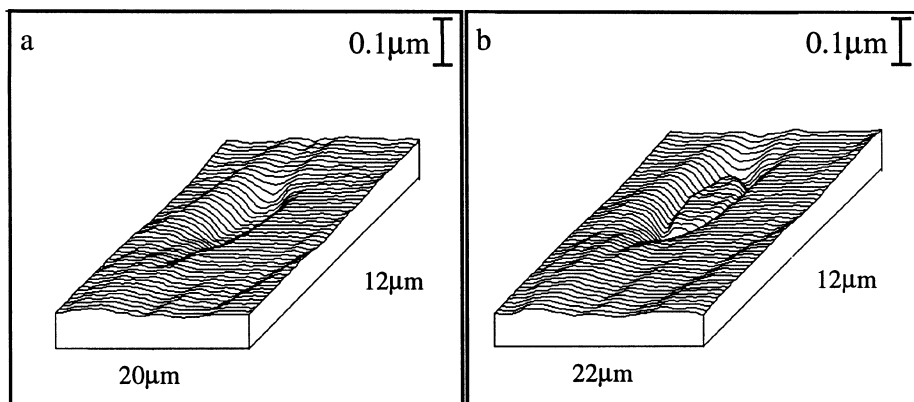


Fig. 10. 3D profiles of an  $\text{Al}_2\text{CuMg}$  particle: a—after polishing; b—after 5 mn of polarization at  $-750 \text{ mV/SCE}$ .

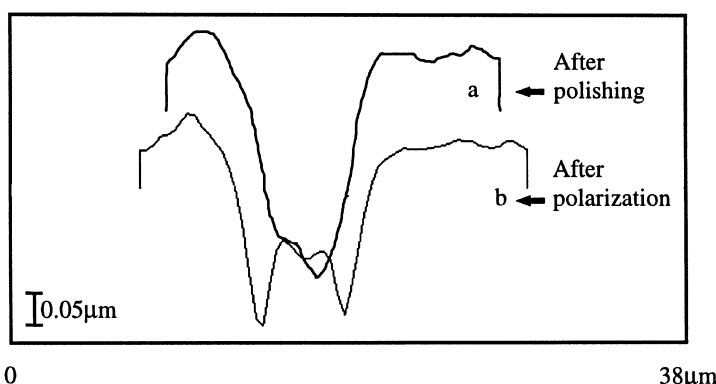


Fig. 11. 2D profiles of the Fig. 10  $\text{Al}_2\text{CuMg}$  particle: a—after polishing; b—after 5 mn of polarization at  $-750 \text{ mV/SCE}$ .

sample is directly polarized at  $-750 \text{ mV}$ , the passive film is not yet formed on the sample surface and consequently the matrix is slightly attacked. The corresponding 2D profile (Figure 11) shows that the dissolution of the matrix surrounding the particle is deeper than the dissolution of the rest of the matrix. Indeed, the surrounding matrix was dissolved by about 80 nm whereas the rest of the matrix lost only about 40 nm. The stronger dissolution of the matrix around the particle explains the impression of the particle inflating. But, in fact, at potentials lower than  $E_{bl}$ , the particle remain unchanged.

These results show that the dissolution of the matrix surrounding the  $\text{Al}_2\text{CuMg}$  particles occurs at potential lower than  $E_{bl}$ . They also show that before  $E_{bl}$ , S phase particles are not attacked. As we showed previously, S phase particles are only attacked on and after  $E_{bl}$  so, the dissolution of the matrix adjacent to the particles is

not a consequence of particle attack. As no other phase was found to be attacked between  $E_{b1}$  and  $E_{b2}$ , the first breakdown potential is assumed to be caused by the preferential dissolution of S phase particles, and the dissolution of  $\text{Al}_2\text{CuMg}$  phase is consequently responsible for anodic current density rise.

To understand the stronger matrix dissolution at the periphery of the S phase particles at potential lower than  $E_{b1}$ , observations by TEM performed on coarse intermetallic particles will be useful. It has been found that  $\text{Al}_2\text{CuMg}$  particles are surrounded by a  $\text{Al}_{20}\text{Mn}_3\text{Cu}_2$  dispersoid-free zone. The dispersoid distribution is very homogeneous in all the rest of the matrix. As dispersoids contain copper, their precipitation depletes the entire matrix of copper; likewise, as S phase particles are rich in copper, their precipitation leads to a preferential depletion of copper in the matrix around them. Actually, the dispersoids contain 15 wt% copper whereas the S phase precipitates contain 38 wt% copper, so the depletion of the matrix surrounding the S phase particles is stronger than the depletion of the rest of the matrix. Indeed, EDX analysis showed that the dispersoid-free zone contains 10–20% less copper than the rest of the matrix. It can be assumed that the preferential dissolution of the matrix surrounding the coarse intermetallic particles is caused by the existence of a galvanic couple between, on the one hand the copper depleted dispersoid-free zone and the rest of the matrix and on the other hand the copper depleted dispersoid-free zone and the  $\text{Al}_2\text{CuMg}$  particles. In fact, S phase particles and the rest of the matrix have both cathodic behaviour in comparison to the copper depleted matrix surrounding the particles. Warner et al. [8] observed the same phenomenon on a 2024 T4.

From these results and observations, it can be inferred that the local dissolution of the matrix surrounding the S phase particles, which occurs at potentials lower than  $E_{b1}$ , is caused by the existence of the following galvanic couples: copper depleted dispersoid-free zone/the rest of the matrix and copper depleted dispersoid-free zone/S phase particles. In both cases, the copper depleted dispersoid-free zone is the more anodic phase. This confirms that preferential dissolution of the matrix surrounding the  $\text{Al}_2\text{CuMg}$  particles is not related to the particle attack, it is only caused by the existence of the galvanic couples. Now, it seems more than likely that  $E_{b1}$  corresponds to the dissolution potential of S phase.

Observation of Al-Cu-Mn-Fe-containing particles by TEM showed that they are also surrounded by a dispersoid-free zone (Figure 4). Consequently, a selective dissolution of the matrix in the vicinity of these particles may also occur. Actually, this preferential dissolution requires much more severe conditions (exposure of the specimen to higher potentials). Yet, the particles always remain practically unattacked (Figure 12).

The dissolution of the matrix surrounding the  $\text{Al}_2\text{CuMg}$  particles seems more rapid and severe than that of the Al-Cu-Mn-Fe-containing particles. Actually, Elboujdaini et al. [15, 16] have shown that the presence of Mg-containing particles has a detrimental effect on the surrounding matrix dissolution and increases this phenomenon. According to these authors, the presence of Mg accelerates the cathodic reaction and leads to the formation of alkaline diffusion layers localized around the particles. Consequently, it appears more natural that the dissolution of the matrix surrounding the S phase particles is stronger than the dissolution of the matrix surrounding the Al-Cu-Mn-Fe-containing particles.

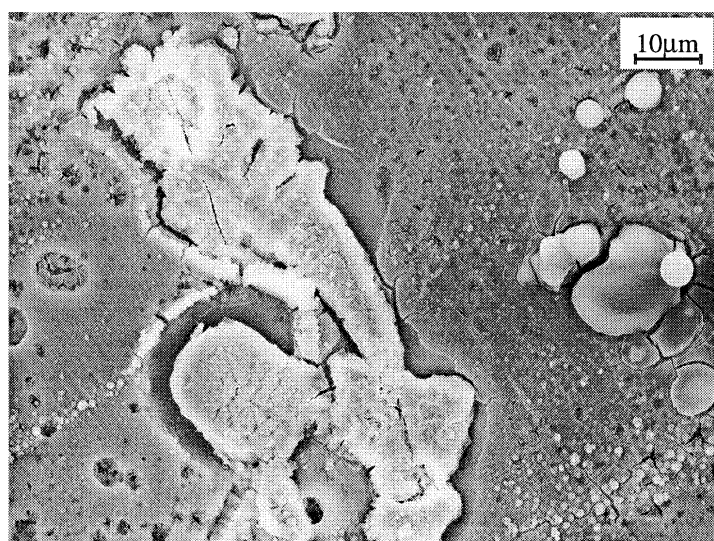


Fig. 12. Al-Cu-Mn-Fe-containing particles after potentiokinetic polarization in 1 M NaCl solution to  $-600\text{ mV/SCE}$ , the potential was maintained at  $-600\text{ mV/SCE}$  for 5 mn.

Finally, the local dissolution of the matrix surrounding the S phase particles is caused by the galvanic couples dispersoid-free zone/the rest of the matrix and dispersoid-free zone/S phase particles; it can occur at low potential whereas the dissolution of the  $\text{Al}_2\text{CuMg}$  particles occurs on and after the first breakdown potential and before the complete dissolution of the particle can lead to the sponge-like structure covered by a more homogeneous layer.

S phase particle behaviour can explain the current density variations observed when a specimen is maintained after the potentiokinetic polarization at a final potential between the first breakdown potential,  $-720\text{ mV}$  and  $-650\text{ mV}$ . Figure 13 shows a typical polarization curve of a specimen polarized from  $-900\text{ mV}$  to  $-650\text{ mV}$  and maintained for 50 mn at  $-650\text{ mV}$ . During the first twenty minutes at  $-650\text{ mV}$ , the anodic current decreases and then begins to oscillate slightly. Ten minutes later, the current clearly fluctuates between cathodic and anodic values. The closer to the breakdown potential the scanning potential is stopped, the sooner the fluctuations begin. For example, if the scanning potential is stopped at  $-690\text{ mV}$ , the oscillations will appear after 8 mn. It has been previously shown that all the particles do not react alike. Some of them can be severely attacked or entirely dissolved whereas others remain unchanged. The oscillations are related to the fact that, at any given moment, not all the particles are active. When few of them are active, the current is anodic. When these active particles are completely dissolved or have fallen out, the corresponding anodic current disappears, at least decreases, and hence the total current is cathodic till other particles begin to dissolve. It can be proposed that the closer the potential is to  $-720\text{ mV}$  when stopped, the smaller the number of active particles, and the sooner oscillations can appear.

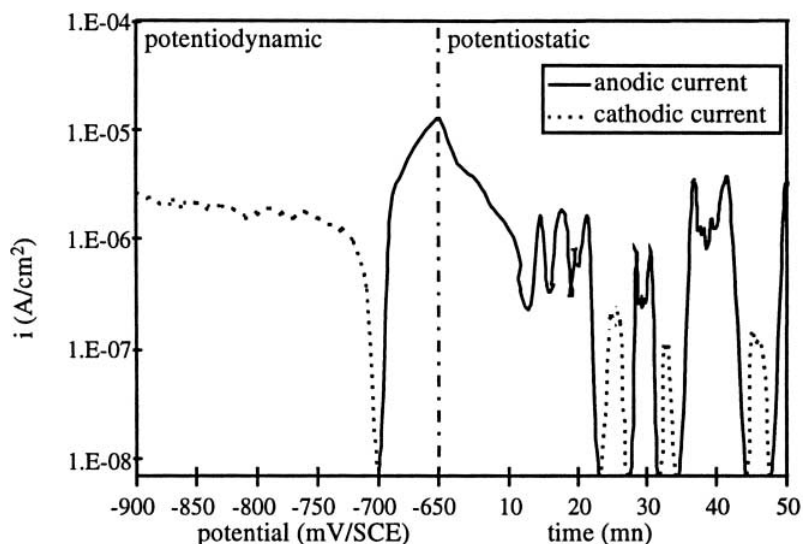


Fig. 13. Potentiokinetic polarization of alloy 2024 T351 from  $-900\text{ mV/SCE}$  to  $-650\text{ mV/SCE}$ , the potential was maintained at  $-650\text{ mV/SCE}$  for 50 mn.

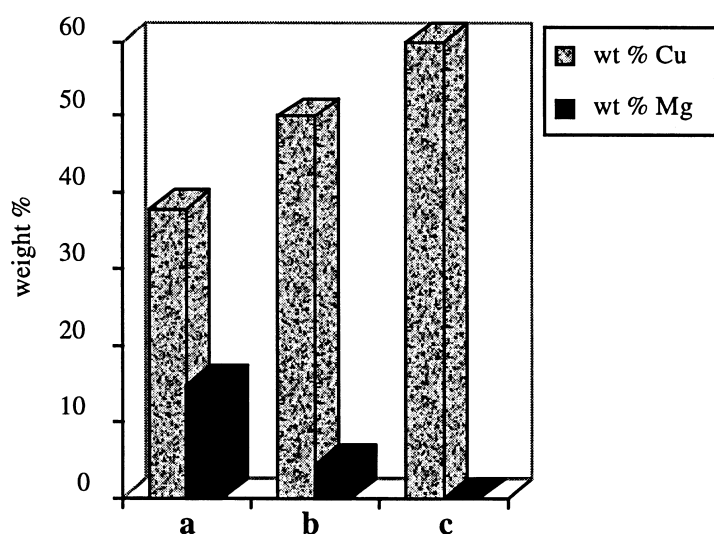


Fig. 14. Weight percent of Mg and Cu in  $\text{Al}_2\text{CuMg}$  particles: a—Before potentiokinetic polarization; b—After potentiokinetic polarization to  $-690\text{ mV/SCE}$  in 1 M NaCl solution at pH 6; c—After the same potentiokinetic polarization in 1 M NaCl solution at pH 2.

EDS analysis of the S phase particles after the potentiokinetic polarization to  $-690\text{ mV}$  shows a depletion of Mg and an enrichment of copper (Figure 14). These analyses were performed on both the porous sponge-like structure and the denser

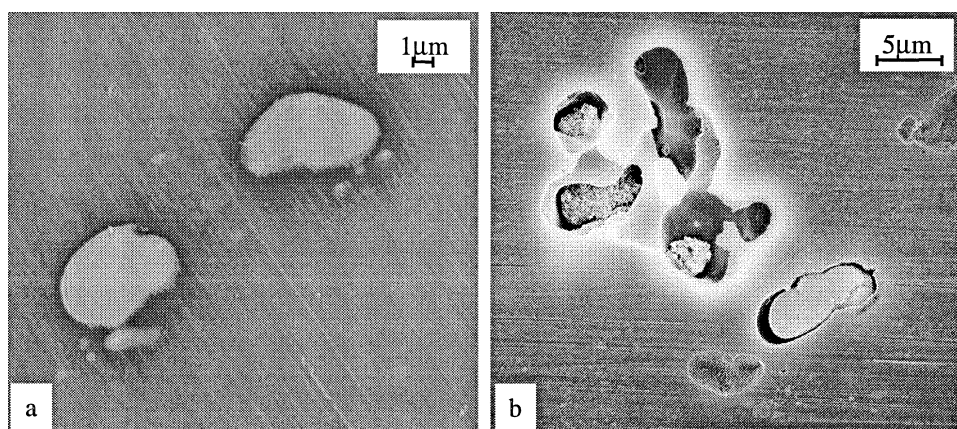


Fig. 15.  $\text{Al}_2\text{CuMg}$  particles after polarization to a potential 30 mV higher than  $E_{\text{bl}}$  in 1 M NaCl at pH 2: a—observation 3 hours after the experiment; b—observation the day after the experiment.

layer: there was no difference. This indicates that Mg selectively dissolves from the  $\text{Al}_2\text{CuMg}$  precipitates leaving Cu-rich remnants. The layer could be a copper deposit resulting from the dissolution of the precipitate followed by immediate deposition of dissolved copper on the particle. Various authors [17–19] have observed the deposition of copper contained in the electrolyte or dissolved from particles. Blanc et al. [11] who worked on 2024 T351 in sulphate media at higher potentials observed a copper deposit on the particle but also around it. Indeed, a copper deposit could explain the copper enrichment of the particle, but a preferential dissolution of Mg could also lead to Cu-rich remnants. Buchheit et al. [7] have also observed a copper enrichment of the S phase particles after immersion of a 2024 T3 alloy in a NaCl solution. They concluded that dealloying of the particle occurred. To make a choice between these two hypotheses, the influence of a few parameters was studied.

Referring to Blanc et al. [11] works, sulphate ions were added to chloride solution in order to examine if copper deposit around the particles could be observed. In these case, copper deposit on the particles would become the preferential hypothesis. But, this experiment was not successful and did not lead to any modification: the layer could always be observed on the particles, but there were no copper deposit around them.

The same potentiokinetic polarization to a potential 30 mV higher than  $E_{\text{bl}}$  was run in a NaCl solution acidified to pH 2. In these more aggressive conditions, observations by SEM made 3 hours after the experiment paradoxically show only a slight attack of the  $\text{Al}_2\text{CuMg}$  particles (Figure 15a). However, some of them had fallen out. One day after this first observation, SEM analyses were performed on the sample. But at that time, the particles seemed to be different and the layer had partially and sometimes completely fallen off (Figure 15b). In fact, at that time the S phase particles really looked like the porous sponge-like structure obtained after polarization to  $-690$  mV at pH 6 (Figure 6). Besides observations in Fig. 7 were made the day after polarization. The EDS analysis of the particles (after polarization at pH 2) shows a

stronger dealloying of Mg, indeed there was no more Mg in the particles, whereas the Cu content had increased Fig. 14. A lot of particles had fallen out. It can be assumed that when the attack is strong, the particle is largely dissolved, the space between the matrix and the particle increases and sometimes the particle falls out.

How could a copper deposit have become altered with time and fallen off? It is most unlikely. On the contrary, a layer with different mechanical properties could be deteriorated during a cycle of  $10^{-7}$  mbar (in the SEM vacuum chamber)/1 bar in natural air (during the night)/ $10^{-7}$  mbar the day after for analysis. Actually, this layer, with a structure which paradoxically appears less porous than the precipitate below, may result from the superficial cold-work caused by mechanical polishing. It also underwent the same Mg dealloying.

### 3.4. Second breakdown potential: pitting corrosion and intergranular corrosion

On and after the second breakdown potential  $E_{b2}$  ( $-620$  mV), both pitting and intergranular corrosion developed. Figure 16 presents several SEM observations of a sample after potentiokinetic polarization to  $-610$  mV (i.e.  $10$  mV higher than the second breakdown potential).

Grain boundaries were attacked and large pits developed within the grains. Some grains were strongly attacked and even the small  $\text{Al}_{20}\text{Mn}_3\text{Cu}_2$  dispersoids seem to be dissolved (Figure 16b and Fig. 16d). The pits showed crystallographic facets. Indeed, a tendency to grow following certain crystal planes can be observed (Figure 16c). Muller et al. [20] previously observed crystallographically shaped pits in the matrix of an Al-3%Cu alloy in 1 M NaCl solutions.

How can the second breakdown potential be related to both pitting and intergranular corrosion? All the authors [2, 14, 20, 21] who have studied intergranular corrosion mechanisms of 2024 alloys or Al-4%Cu alloys showed that intergranular corrosion was caused by the dissolution of the copper-depleted zone along the grain boundaries. This copper-depleted zone only contains 0.2% Cu. However, Fig. 2 shows that no precipitate-free zone was observed along the grain boundaries of the 2024 T351 alloy. Yet, EDS analysis of the grain boundary show that it only contains 3 wt% Cu (such accurate analysis was possible with the JEOL 2010 apparatus which allows the utilization of a 7 nm analysis spot). The same copper content was found over a zone of 20 nm wide on both sides of the grain boundary. Consequently, the grain boundary presented as light depletion in copper in comparison with the rest of the matrix which contained 4 wt% copper.

It was seen that two types of precipitate can be encountered in the grain boundary: the  $\text{Al}_2\text{CuMg}$  hardening precipitates Figure 5, and the bigger  $\text{Al}_2\text{CuMg}$  needle shaped precipitates Figure 6. It was also seen that the dissolution of the  $\text{Al}_2\text{CuMg}$  coarse intermetallic particles starts at  $-720$  mV, so the dissolution of the  $\text{Al}_2\text{CuMg}$  grain boundary precipitates whose chemical phase is the same as that of the coarse intermetallic particles, probably occurs at a potential close to  $-720$  mV. Yet, before  $E_{b2}$ , the alloy is not susceptible to intergranular corrosion, so intergranular precipitate dissolution does not immediately lead to intergranular attack. So, it can be assumed that  $E_{b2}$  only corresponds to the matrix breakdown potential since pits can be observed

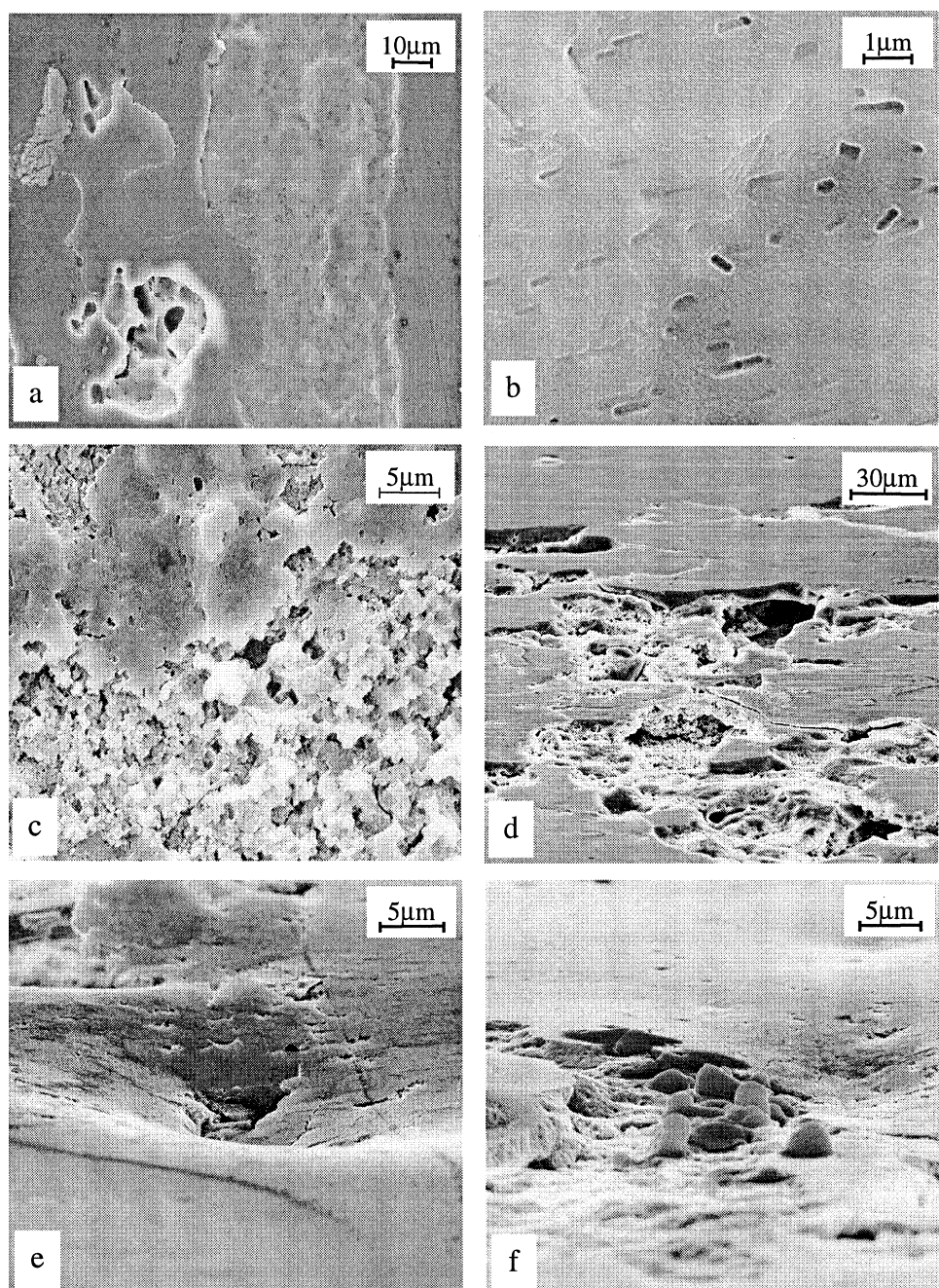


Fig. 16. 2024 T351 surface after potentiokinetic polarization to  $-610\text{ mV/SCE}$ , the potential was maintained at  $-610\text{ mV/SCE}$  for 5 mn; d, e and f were taken with an  $88^\circ$  tilt.

on the sample surface, but it also allows intergranular corrosion to develop. After  $E_{b2}$ , grain boundaries could be the preferential sites for the attack in so far as, the previous dissolution of the intergranular precipitates makes the intergranular sites fragile, and also, grain boundaries are more anodic in comparison to the rest of the matrix since they only contain 3 wt% Cu.

Urushino et al. [14] who studied the intergranular stress corrosion cracking of 2024 analysed the behaviour of the intermetallic compound  $\text{Al}_2\text{CuMg}$  in 1 M NaCl. They showed that its dissolution starts at  $-880$  mV. It seems obvious the anodic dissolution of the  $\text{Al}_2\text{CuMg}$  coarse intermetallic particles, and that of the  $\text{Al}_2\text{CuMg}$  grain boundary precipitates cannot occur at exactly the same potential since all these phases differ. Coarse intermetallic particles can be encountered in the alloy matrix before the heat treatment whereas grain boundary precipitates are formed during the heat treatment. Their sizes are very different ( $20\ \mu\text{m}$  for the coarse particle and around  $1\ \mu\text{m}$  for the others), and their chemical composition might not be exactly the same. Urushino et al. [14] found that the anodic dissolution of the intermetallic compound starts at  $-880$  mV. It has been found in the present study that the anodic dissolution of the  $\text{Al}_2\text{CuMg}$  coarse intermetallic particles starts at  $-720$  mV. Consequently, the anodic dissolution of the  $\text{Al}_2\text{CuMg}$  grain boundary precipitates might occur between these two potentials, or around them. Anyway, in both cases ( $-880$  mV or  $-720$  mV), the two potentials are lower than  $E_{b2}$ , so the intergranular precipitates are already dissolved when the potential reaches  $-620$  mV.

This is why pitting and intergranular corrosion develop on and after the same breakdown potential which corresponds to the dissolution of the matrix both in the grains and in the grain boundaries where precipitates have already been dissolved.

#### 4. Conclusion

The potentiokinetic polarization curve of alloy 2024 T351 presents two breakdown potentials. The more active one, occurring around  $-720$  mV, is caused by the selective dissolution of the S phase particles. A severe Mg dealloying of the particles results in Cu-rich remnants. The  $\text{Al}_2\text{CuMg}$  particles are surrounded by a dispersoid-free zone. hence the galvanic couples dispersoid-free zone/the rest of the matrix and dispersoid-free zone/S phase particles cause the dissolution of the matrix surrounding the particles. The more noble one occurring around  $-620$  mV corresponds to the dissolution of the matrix and the dissolution of the grain boundaries. Both pitting and intergranular corrosion develop. This potential seems to correspond to the matrix breakdown potential. It also allows intergranular corrosion to develop. Grain boundaries are susceptible to preferential dissolution because they are more anodic in comparison to the rest of the matrix and the dissolution of the intergranular precipitates (around  $-720$  mV) makes them fragile.

#### Acknowledgements

This work was carried out in the framework of the ‘Laboratoire Régional pour l’Amélioration des Matériaux Structuraux pour l’Aéronautique’ with the financial

support of the Région Midi-Pyrénées. Special recognition goes to Michelle Reversat and Djar Oquab for the SEM work. Josette Poujardieu for TEM work and Yves Roques for PSIM work.

## References

- [1] H.P. Godard, W.B. Jepson, M.R. Bothwell, R.L. Kane, *The Corrosion of Light Metals*, J. Wiley and Sons Inc., New York, 1967, pp. 70–73.
- [2] J.R. Galvele, S.M. de Micheli, *Corros. Sci.* 10 (1970) 795.
- [3] D.E. Davies, J.P. Dennison, M.L. Mehta, in: R.W. Staehle et al. (Eds.), *International Conference on Localized Corrosion*, National Association of Corrosion Engineers, Houston, TX, 1971, pp. 608–613.
- [4] P. Doig, P.E.J. Flewitt, J.W. Edington, *Corrosion* 33 (1977) 217.
- [5] S. Maitra, G.C. English, *Metallurgical Transactions A* 12A (1981) 535.
- [6] R. Escalona, R. Devillers, G. Tribillon, J. Calatroni, P. Fievet, Y. Roques, F. Dabosi, *J. Mater. Sci.* 28 (1993) 299.
- [7] R.G. Buchheit, R.P. Grant, P.F. Hlava, B. Mckenzie, G.L. Zender, *J. Electrochem. Soc.* 144 (1997) 2621.
- [8] T.J. Warner, M.P. Schmidt, F. Sommer, D. Bellot, *Z. Metallkd.* 86 (1995) 494.
- [9] S. Berrada, E. Ghali, *Canadian Metallurgical Quarterly* 33 (1994) 359.
- [10] S. Berrada, M. Elboujdaini, E. Ghali, *J. of Appl. Electrochem.* 22 (1992) 1068.
- [11] C. Blanc, B. Lavelle, G. Mankowski, *Corros. Sci.* 39 (1997) 495.
- [12] L.F. Mondolfo, *Aluminium Alloys: Structure and Properties*, Butterworths, London, 1976, pp. 693–758.
- [13] B. Dubost, P. Sainfort, *Techniques de l'Ingénieur, M1II, Matériaux Métalliques, Etudes des Alliages M240* (1991) 00.
- [14] K. Urushino, K. Sugimoto, *Corros. Sci.* 19 (1979) 225.
- [15] M. Elboujdaini, E. Ghali, *Corros. Sci.* 30 (1990) 855.
- [16] M. Elboujdaini, E. Ghali, R.G. Barradas, M. Girgis, *J. of Appl. Electrochem.* 25 (1995) 412.
- [17] M.G.A. Khedr, A.M.S. Lashien, *Corros. Sci.* 33 (1992) 137.
- [18] H. Böhni, H.H. Uhlig, *J. Electrochem. Soc.* 116 (1969) 906.
- [19] B. Mazurkiewicz, A. Piotrowski, *Corros. Sci.* 23 (1983) 697.
- [20] I.L. Muller, J.R. Galvele, *Corros. Sci.* 17 (1977) 179.
- [21] A. Garner, D. Tromans, *Corrosion* 35 (1979) 55.